Mon. Not. R. Astron. Soc. **295,** 860–868 (1998)

# Two serendipitous low-mass LMC clusters discovered with *HST*

Basílio X. Santiago,[1,2] Rebecca A. W. Elson,[2] Steinn Sigurdsson[2] and Gerard F. Gilmore[2]

[1] *Departamento de Astronomia, Universidade Federal do Rio Grande do Sul, 91501-970, Porto Alegre, RS, Brasil*
[2] *Institute of Astronomy, Cambridge University, Madingley Road, Cambridge CB3 0HA*

Accepted 1997 November 20. Received 1997 September 23; in original form 1997 May 16

**ABSTRACT**

We present $V$ and $I$ photometry of two open clusters in the LMC down to $V \sim 26$. The clusters were imaged with the Wide Field and Planetary Camera 2 (WFPC2) on board the *Hubble Space Telescope* (*HST*), as part of the Medium Deep Survey Key Project. Both are low-luminosity ($M_V \sim -3.5$), low-mass ($M \sim 10^3$ M$_\odot$) systems. The chance discovery of these two clusters in two parallel WFPC2 fields suggests a significant incompleteness in the LMC cluster census near the bar. One of the clusters is roughly elliptical and compact, with a steep light profile, a central surface brightness $\mu_V(0) \sim 20.2$ mag arcsec$^{-2}$, a half-light radius $r_{\rm hl} \sim 0.9$ pc (total visual major diameter $D \sim 3$ pc) and an estimated mass $M \sim 1500$ M$_\odot$. From the colour–magnitude diagram and isochrone fits we estimate its age as $\tau \sim (2\text{–}5) \times 10^8$ yr. Its mass function has a fitted slope of $\Gamma = \Delta \log \phi(M)/\Delta \log M = -1.8 \pm 0.7$ in the range probed ($0.9 \lesssim M/{\rm M}_\odot \lesssim 4.5$). The other cluster is more irregular and sparse, having shallower density and surface brightness profiles. We obtain $\Gamma = -1.2 \pm 0.4$, and estimate its mass as $M \sim 400$ M$_\odot$. A derived upper limit for its age is $\tau \lesssim 5 \times 10^8$ yr. Both clusters have mass functions with slopes similar to that of R136, a massive LMC cluster, for which *HST* results indicate $\Gamma \sim -1.2$. They also seem to be relaxed in their cores and well contained in their tidal radii.

**Key words:** stars: luminosity function, mass function – stars: statistics – Magellanic Clouds – galaxies: star clusters.

## 1 INTRODUCTION

The Large Magellanic Cloud (LMC) contains a vast number of star clusters, with ages ranging from $10^7$ to $10^{10}$ yr. The LMC cluster system is thus suitable for studying the evolution of physical properties of clusters such as mass, radius, light and density profiles, luminosity functions (LFs) and mass functions (MFs). These latter may depend not only on age, but also on metal abundance or environment, and provide relevant information on the physics of star formation from fragmenting gas clouds (McClure et al. 1986; Larson 1991, 1992).

Derivation of relevant physical parameters in LMC clusters, as well as in other dense stellar systems, has been limited by lack of spatial resolution. This situation improved considerably with the refurbishment of the *Hubble Space Telescope* (*HST*), allowing crowding problems in dense stellar systems to be substantially reduced (de Marchi & Paresce 1995a,b; Elson et al. 1995; Hunter et al. 1996; Santiago, Elson & Gilmore 1996). However, the faint end of the cluster LF in the LMC has not yet been targeted by deep photometric studies. *HST* imaging of clusters and associations published so far has concentrated on Galaxy clusters or on rich systems in the Local Group. Almost nothing is known about small LMC clusters, whose detection is often difficult and whose properties are harder to determine observationally. The LF of LMC clusters seems to rise steeply in the low-luminosity domain (Elson & Fall 1985). In fact, the total number of detected LMC clusters has been steadily increasing, and is currently believed to be about $\sim 4500$ (Hodge 1988).

In this paper we report observations of two low-luminosity ($M_V \sim -3.5$) clusters in the LMC. They were detected in two parallel Wide Field and Planetary Camera 2 (WFPC2) images as part of the Medium Deep Survey *HST* Key Project (MDS). This chance discovery of two clusters suggests that such objects may be very common in the LMC. If our two MDS fields are typical, the implied surface density would be considerably larger than that inferred by Elson & Fall (1985) or by the deep photographic study of Hodge (1988), at least in the vicinities of the LMC bar or the 30 Doradus region.

In Section 2 we present *HST* photometry in two bands for the two MDS fields; we show colour–magnitude diagrams (CMDs) and discuss completeness corrections and photometric calibration issues. We then use the data to extract surface brightness and stellar density profiles for the clusters, and to estimate their ages (Section 3). In Section 4 we compute their LFs and MFs. We also briefly discuss their dynamical state. In Section 5 we discuss the results and present our conclusions.

## 2 THE DATA

### 2.1 Data reduction

The two LMC fields studied in this work were imaged in parallel mode with WFPC2, as part of the MDS project. Field 1 is located at $\alpha = 0.5^{\rm h}35^{\rm m}36\overset{\rm s}{.}8$, $\delta = -69°24'23''$ (J2000). Field 2 is located at $\alpha = 05^{\rm h}36^{\rm m}52\overset{\rm s}{.}3$, $\delta = -69°37'59\overset{''}{.}6$ (J2000). Both fields are at the eastern end of the LMC bar, south-west of 30 Doradus, close to NGC 2050 and 2048, respectively. Each field contains one of the small clusters reported in this work. We hereafter refer to the cluster located in field 1 (field 2) as C1 (C2).

Field 1 was imaged with two 500-s exposures using the *HST* F814W (*I*) filter, and two 500-s exposures with the *HST* F606W (*V*) filter. For field 2, two exposures in each filter were also taken: 4900 and 1100 s in F814W, and 5900 and 1000 s in F606W.

The raw data were processed with the standard pipeline procedure, which corrects for instrumental effects (Holtzmann et al. 1995a). The two exposures in each field/filter combination were then co-added and median-filtered; the lower instrumental value was used at each pixel position to eliminate cosmic rays. Field 2 F814W frames were offset by about 3 arcsec from each other, and were registered to a common position before co-adding.

### 2.2 Sample selection

An object list was obtained separately for each field/filter configuration from the final co-added image. The IRAF DAOPHOT package (Stetson 1987) was used for this as well as for aperture and point-spread function (psf) fitting photometry. We adopted a detection threshold of $3\sigma$, where $\sigma$ is the standard deviation in the background counts of each chip. We worked only with the three Wide Field Camera 2 (WFC2) chips, since the Planetary Camera (PC) chip would not significantly increase the sample size.

Inspection of the images showed that most of the objects detected were real stars. However, some spurious detections occurred, especially around bright stars. In order to clean up the sample, a psf template was created from a few bright unsaturated stars in each WFC2 chip and then fitted to all remaining objects using ALLSTAR. This task gives a value of $\chi^2$ and a sharpness parameter ($s$). The dependence of these parameters on the $V_{606}$ magnitude for chip 4, field 1 is shown in Fig. 1. There are two loci in the sharpness diagram: inspection of the images revealed that the clump of objects with $s > 0.1$ contains predominantly spurious detections (also attested by their large $\chi^2$), whereas the low-sharpness locus was almost entirely made up of stars. An additional cut in $\chi^2 < 2$ was also applied to eliminate the few remaining objects whose fit to the psf template was not satisfactory. Also, in order to avoid saturation effects, all objects brighter than $I_{814} = 18$ or $V_{606} = 19$ were eliminated. Fig. 1 is typical of the other two WFC2 chips in field 1, both for F606W and for F814W.

Field 2 has a longer exposure time, leading to enhanced crowding and more saturated stars. The saturation magnitudes measured for field 2 are $I_{814} = 20.5$ and $V_{606} = 21.5$. Registration of the F814W images reduced the quality of the psf fits. The $s$ versus $I_{814}$ and $\chi^2$ versus $I_{814}$ diagrams did not display as clear boundaries between stellar and non-stellar objects. Star selection for field 2 was therefore restricted to the F606W image, although object detection was carried out independently in both filters. The faint saturation limits in field 2 made it difficult to select bright stars based on the $\chi^2$ versus $V_{606}$ and $s$ versus $V_{606}$ diagrams. Thus only stars with $V_{606} \gtrsim 21.5$ were selected in this way. Brighter stars were selected from a smoothed version of the co-added images, obtained by applying a 3-pixel ($\sim 0.3$ arcsec) Gaussian. This filter is wide enough to eliminate hot pixels and psf features, but narrow enough to allow the detection of bright objects.

The number of stars was typically 6000–7000 per chip in field 1, and 8000 in field 2. Of these, about 5000 had *both* $I_{814}$ and $V_{606}$ magnitudes available.

### 2.3 Photometry

Even though sample selection was mostly based on psf fitting, the magnitudes and colours used in the analysis came from aperture photometry inside a radius $r = 2$ pixel ($r = 0.2$ arcsec). $V_{606}$ and $I_{814}$ magnitudes measured in this way led to a narrower CMD than that based on the psf magnitudes. The choice of radius is a compromise between the need to bypass centring and undersampling problems and the need to avoid light contamination from neighbouring sources. An aperture correction of 0.24 mag had to be applied to both *HST* filters in order to account for the light outside the aperture (Holtzmann et al. 1995a).

For field 2, saturation prevented magnitudes and colours of upper main sequence and red giant branch (RGB) stars to be measured. In order to bypass this problem, aperture photometry for the bright stars in field 2 ($V_{606} < 21.5$) was carried out in the F814W and F606W frames with the shortest exposure time. These have much less stringent saturation limits ($I_{814} \sim 18.75$, $V_{606} \sim 19.75$).

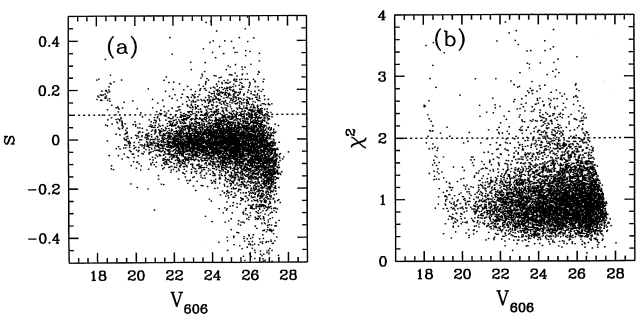


**Figure 1.** The sharpness ($s$) and $\chi^2$ parameters, as obtained by fitting each detected object in chip 4, field 1 to the WFC2 psf, are shown as a function of $V_{606}$ magnitudes. (a) $s$. (b) $\chi^2$.

Finally, an attempt was made to measure magnitudes for field 2 stars with $I_{814} < 18.75$ or $V_{606} < 19.75$ using only the pixels within the circular ring between 2- and 3-pixel radius. Again the shortest exposures were used. Given the shape of the WFC2's psf, this in principle allows one to push saturation levels towards brighter magnitudes. The quality of the magnitudes obtained with this procedure was tested with several isolated, bright and unsaturated stars. Only approximate magnitudes could be measured, the uncertainty being $\sim 0.35$ mag. About 50 such bright stars were added to the sample in each field 2 chip.

### 2.4 Photometric calibration

The data were calibrated to the Johnson–Cousins system using the 'synthetic' transformation equation listed in table 10 of Holtzmann et al. (1995b).

Reddening corrections were determined by comparing isochrones and the aperture-corrected instrumental CMDs until the observational and theoretical main sequences and RGBs coincided. We used Yale isochrones for that purpose (Green, Demarque & King 1987), and assumed a distance modulus of $m - M = 18.5$ to the LMC (Panagia et al. 1991). The Yale isochrones had first to be converted to the *HST* photometry system by applying the inverse of the calibration equations listed by Holtzmann et al. (1995b). For field 1, $E(V_{606} - I_{814}) = 0.12$ was obtained. For field 2, $E(V_{606} - I_{814}) = 0.17$ provided the best fit. Given the difficulty in fitting all the CMD features, however, these values may be uncertain by as much as 0.1 mag.

The reddening and aperture-corrected *HST* CMDs for all stars in fields 1 and 2 are shown in Fig. 2. Also shown are Yale isochrones for $Z = 0.01$ stars with ages of 0, 200, 500, 1000 and 2000 Myr. Only non-saturated stars are included. The CMD for field 1 (panel a) shows a main sequence ranging from $V_{606} \sim 18.5$ down to $V_{606} \sim 26$. The RGB is also clearly visible in both panels, but especially for field 1, where the shorter exposure time and the more accurate sample selection and photometry allow even the red giant clump ($V_{606} \sim 18.5$–19) to stand out. The larger number of objects in field 2 which lie outside the main sequence and RGB reflects the limitation in star selection, which for field 2 was based on the F606W image only.

The isochrones nicely fit the main sequences of both panels, justifying the adopted reddening and distance modulus. In particular, the isochrones bracket the width of the upper main sequence, which should be made up of fairly young stars and for which the choice of metallicity is justified (Olszewski et al. 1991). A detailed analysis and discussion of the field stellar populations and star formation history in these fields was left to Elson et al. (1997).

### 2.5 Completeness corrections

Completeness functions were obtained independently for field and cluster stars, since they are known to depend on crowding. Completeness functions were measured mostly for WFPC2 chip 4, field 1 and WFPC2 chip 3, field 2, where C1 and C2 are respectively located.

For the field stars, we ran a total of 40 realizations of the DAOPHOT.ADDSTAR task for each *HST* filter, five realizations for each of eight magnitude bins, spanning the range

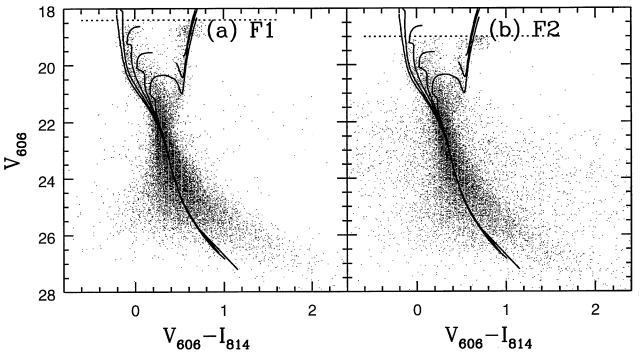


**Figure 2.** (a) CMD for all three WFC2 chips in field 1. The magnitudes and colours are in the *HST* WFPC2 system. The data are corrected for aperture and reddening effects. Superposed are Yale isochrones corresponding to $Z = 0.01$ stars with ages 0, 200, 500, 1000 and 2000 Myr. (b) The same as in (a), but now for the three WFC2 chips in field 2.

$20 \leq I_{814}, V_{606} \leq 28$. In each realization, 200 stars were added to randomly chosen sections of the original frame, each section being $400 \times 400$ pixel wide and situated away from the cluster. The section images containing the artificial stars were then put through the same detection and star classification processes as the real data. Only artificial stars whose input and observed magnitudes were within 0.3 mag of each other were considered as detected. The average fraction, out of the five realizations for each magnitude bin, of artificial objects detected and classified as stars was taken as the completeness value at that magnitude.

For the cluster regions we made 40 realizations with 10 artificial stars for each of 12 magnitude bins within the range $20 \leq I_{814}, V_{606} \leq 26$. Experiments showed that C1 completeness does not depend strongly on position within the cluster region. This is consistent with the compact and steeply declining profile for this cluster (Section 3). For C2, two completeness functions were assigned, one for its core region and the other for the outskirts.

The $V_{606}$ completeness functions are shown in Fig. 3. Cluster completeness falls more rapidly with magnitude than field completeness due to more severe crowding. The differences in completeness between fields 1 and 2 are almost always smaller than the error bars. This applies both to cluster and field stars completeness functions.

A faint cut-off limit was applied to the data in order to avoid large shot-noise errors. Magnitude limits of $I_{814} = 25$ ($I_{814} = 24$) and $V_{606} = 26$ ($V_{606} = 25$) were applied to field (cluster) stars. The magnitude errors ($1\sigma$) at the cut-off limits are $\delta I_{814} \sim 0.2$ for $I_{814} = 25$ and $\delta V_{606} \sim 0.3$ for $V_{606} = 26$. These limits were used in the derivation of structural parameters, density and surface brightness profiles, LFs and MFs presented in Sections 3 and 4.

The $I_{814}$ completeness functions behave similarly to the ones shown in Fig. 3. Since the final sample used in this work is that made up of objects with both a $V_{606}$ and an $I_{814}$ magnitude, a joint completeness function has computed. The additional incompleteness caused by the requirement of $V$- ($I$-) band detection was quantified by simply multiplying, at each magnitude level, the $I$ ($V$) completeness function, by the fraction of sources detected (and classified as stars) in $I$ ($V$) which made into the final sample.

## 3 THE LOW-MASS LMC CLUSTERS: MORPHOLOGY, STRUCTURE AND AGE

### 3.1 Morphology and structure

$V_{606}$-band images of C1 and C2 are shown in Figs 4 and 5. C1 is located at $\alpha = 0.5^h 35^m 35\overset{s}{.}1$, $\delta = -69°23'48\overset{''}{.}8$, whereas C2's centre is at $\alpha = 0.5^h 36^m 51\overset{s}{.}9$, $\delta = -69°38'12\overset{''}{.}1$ (J2000). These positions are about 20 and 30 arcmin away from the centre of the 30 Dor region, respectively.

C1 has visually determined major and minor diameters of $12 \times 10$ arcsec$^2$. Assuming a distance modulus of $m - M = 18.5$ for the LMC, this corresponds to $D \times d \sim 3 \times 2.5$ pc$^2$ (1 pc $\equiv$ 4.1 arcsec).

In Fig. 6 we show the stellar number density (panel a) and the surface brightness profiles (panel b) for C1. The upper curve in both panels gives the profile uncorrected for contamination by field stars. The error bars include Poission fluctuations as well as uncertainties in the completeness functions. The dots show background-corrected profiles and incorporate the additional statistical uncertainty associated with the subtracted background stars. Arrows indicate upper limits. In this case the tip of the arrow is at the most probable value, and its upper end correspondsd to the $1\sigma$ deviation from this value. The horizontal lines in both panels indicate the background levels, determined separately for each WFC2 chip (dotted lines), and linearly interpolated into the cluster region (solid line). This latter was used as the best estimate of the field contamination at the cluster

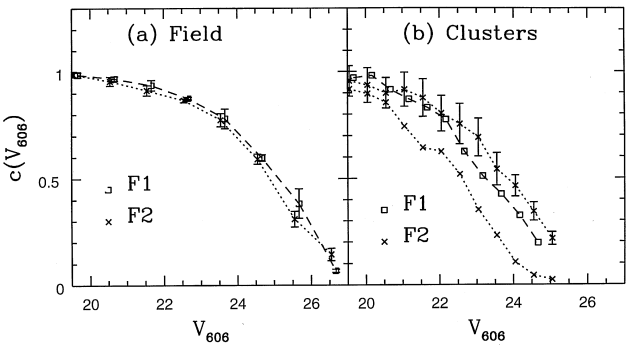


**Figure 3.** (a) $V_{606}$ completeness functions for field stars in field 1, chip 4 (squares and dashed line) and in field 2, chip 3 (crosses and dotted line). Error bars are standard deviations from different realizations of ADDSTAR, as explained in the text. (b) Same as in (a), but now cluster completeness functions are shown: squares and dashed line: C1; crosses and dotted lines: inner and outer C2. Error bars are shown only for one of the cluster completeness functions to avoid confusion.

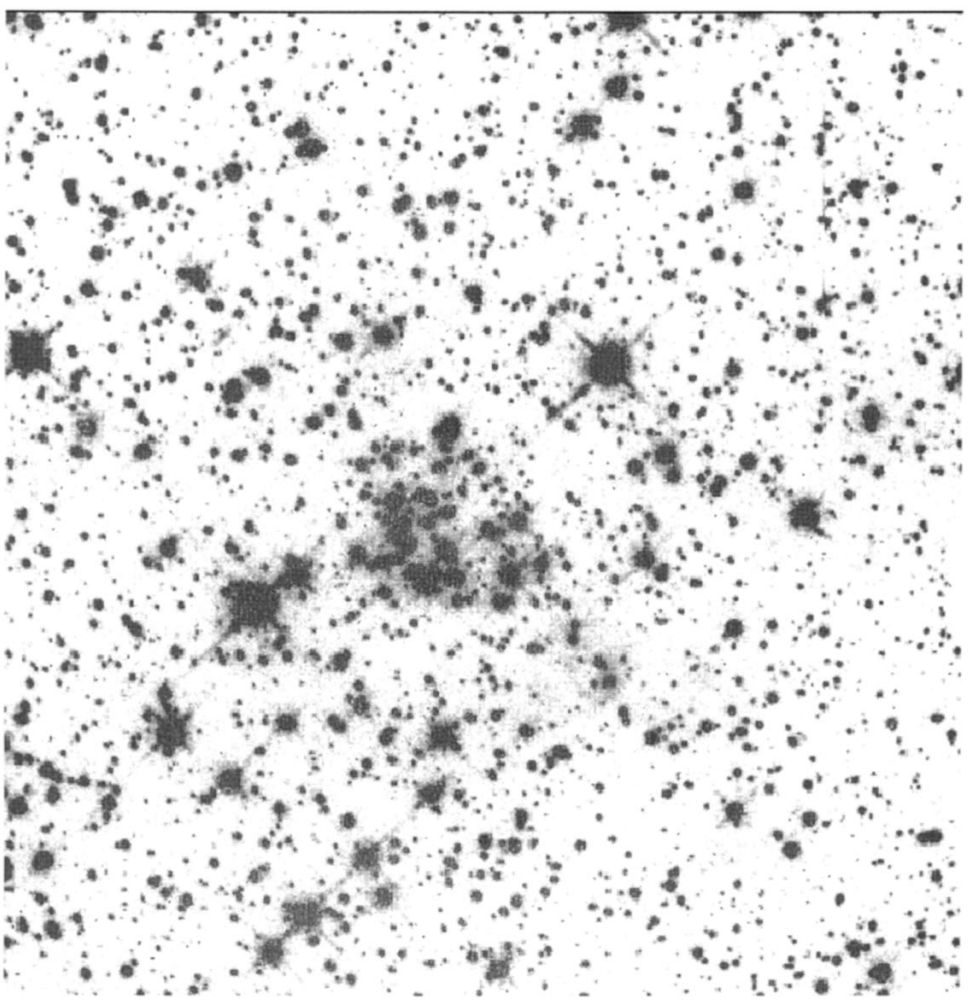

**Figure 4.** WFPC2 image of LMC field 1 cluster, C1. The whole field shown is about 50 arcsec on a side.

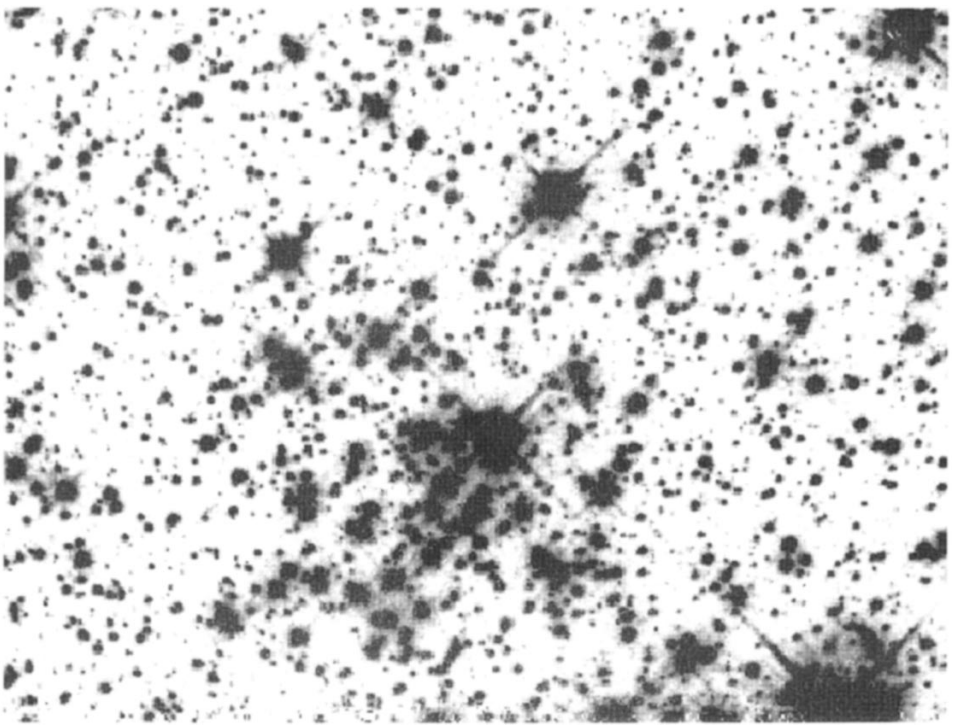

**Figure 5.** WFPC2 image of LMC field 2 cluster, C2. The whole field shown is about 40 arcsec on a side.

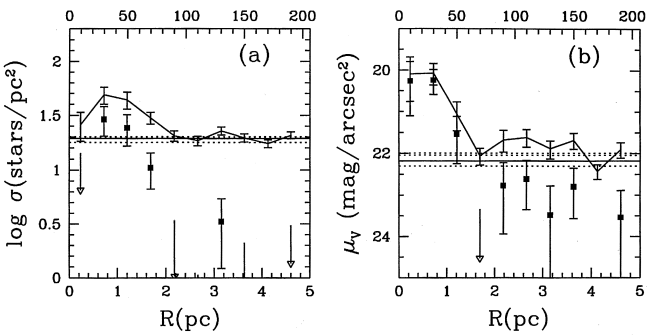


**Figure 6.** (a) Stellar density profile within the region occupied by C1. The upper curve gives the surface density of stars as a function of distance from the cluster centre, without any correction for field contamination. The points indicate the background-corrected profile. Arrows correspond to upper limits. The adopted background density level is given by the solid horizontal line. The dotted horizontal lines show the background densities estimated separately for each WFC2 chip. (b) *V*-band surface brightness profiles and background levels corresponding to the number density ones shown in panel (a).

position. The profiles shown include only stars in the range $-0.5 \leq M_V \leq 6.5$.

A clear excess of stars is visible out to $R \sim 2$ pc ($\sim 80$ pixel), beyond which the stellar numbe density merges with that estimated for the LMC field (panel a of Fig. 6). There are at least as many cluster stars as background stars within this radius. C1's central regions have a roughly constant surface brightness, $\mu_V \sim 20.2$ mag arcsec$^{-2}$ (panel b of Fig. 6). Beyond $R \sim 0.5$ pc, however, the surface brightness profile falls steeply with radius, flattening out again at $R \sim 2$ pc. This outer extension is not visually noticeable (see Fig. 4), and is not present in the number density profile either (panel a of Fig. 6). It could be an artefact caused by underestimation of background surface brightness levels; as panel (b) itself shows, the background field $\mu_V$ varies by some 0.3 mag arcsec$^{-2}$ with position within field 1. However, the uncorrected $\mu_V$ profile is still brighter than the highest background level estimated from the WFC2 chips. Since C1 lies in an intersection of several associations and star-forming regions, the excess of surface brightness beyond $R \sim 2$ pc may be caused by these larger scale structures in the LMC. We return to this issue in Section 4.1.

The stellar density and surface brightness profiles for C2 are shown in Fig. 7. Again only stars with $-0.5 \leq M_V \leq 6.5$ contribute to the profiles. Because C2 is closer to the chip border than C1, its profiles do not extend as far from the cluster centre as in the case of C1. C2 has visual diameters of $19 \times 16$ arcsec$^2$ ($D \times d = 4.6 \times 3.9$ pc$^2$). Its visual appearance suggests a sparser and more irregular cluster showing some substructure. In spite of the low stellar number density contrast relative to the background, panel (a) of Fig. 7 shows a systematic excess of stars out to $R \sim 1.5$ pc, although this excess is hardly significant beyond $R \sim 1$ pc. C2's light profile (panel b), on the other hand, is above that of the contaminating field out to $R \sim 1.5$ pc, the excess brightness relative to the background being still significant all the way out to the edge of the chip. We get $\mu_V(0) \sim 20.3$ mag arcsec$^{-2}$ for C2, comparable to C1. Its $\mu_V$ profile is shallower than that of C1.

The inferred structural parameters for C1 and C2 are listed in Table 1, including sizes and central densities.

### 3.2 Ages

The top panels of Fig. 8 show the CMDs for stars within boxes of 16 arcsec (4 pc) on a side centred on C1 (panel a)

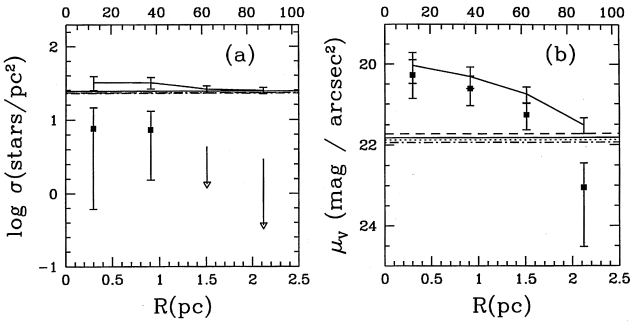


**Figure 7.** (a) The same as in Fig. 6(a), but now for C2. (b) The same as in Fig. 6(b), but now for C2.

**Table 1.** Structural parameters of clusters.

| Parameter | C1 | C2 |
|---|---|---|
| $\sigma_0$ (stars/pc$^2$) | $30 \pm 8$ | $8 \pm 6$ |
| $R_\sigma$ (pc) | $\sim 2$ | $\sim 1.5$ |
| $\mu_V(0)$ (mag/arcsec$^2$) | $20.2 \pm 0.4$ | $20.3 \pm 0.5$ |
| $R_\mu$ (pc) | $\sim 2$ | $\sim 2$ |
| $R_{hl}$ (pc) | $\sim 0.9$ | $\sim 0.7$ |
| $D_{vis} \times d_{vis}$ (pc) | $2.9 \times 2.4$ | $4.6 \times 3.9$ |
| $\tau(Myrs)$ | 200-500 | $\lesssim 500$ |

and on C2 (panel b). A total of 268 and 310 stars are shown in panels (a) and (b), respectively. The data are in the Johnson–Cousins system and are corrected for aperture and extinction effects, as described in Sections 2.3 and 2.4. The dashed lines indicate saturation levels. They correspond to a fixed $V_{606}$ cut-off (see Sections 2.2 and 2.3). The lower panels show CMDs for stars in the neighbourhood of each cluster, for comparison. The entire area outside the cluster in the WFC2 chip where it is located was used as comparison field. The field CMDs shown include a randomly selected fraction of the field stars, so that the numbers of cluster and background stars in any region of the CMD can be directly compared. They clearly differ in the upper main sequence: there are 16 main-sequence stars with $V < 20$ in panel (a), eight of which have $V < 19$. In the corresponding comparison field (panel c), these numbers are eight and one. Similarly, only three main-sequence stars have $V < 20$ in panel (d), whereas in the corresponding cluster CMD there are 14 such stars. Thus most of the upper main-sequence stars are real cluster members, and we expect field contamination not to affect age estimates from isochrone fitting.

Yale isochrones corresponding to $Z = 0.01$ stars with ages of 0, 200, 500, 1000 and 2000 Myr are shown in the upper panels. This chosen metallicity is typical of LMC clusters (Olszewski et al. 1991). Its associated uncertainty ($\delta$[Fe/H] $\sim 0.15$) has a smaller effect on the isochrone fits than the reddening and saturation effects. The 500-Myr isochrone is the one that best fits C1's upper main sequence. However, a few saturated stars existed within C1 and have been left out of Fig. 8. The presence of stars brighter than the 500-Myr turn-off would indicate a lower age. In fact, adjustments in the amount of extinction or in the metallicity assumed for the stars would allow an age as low as $\tau = 200$ Myr for C1.

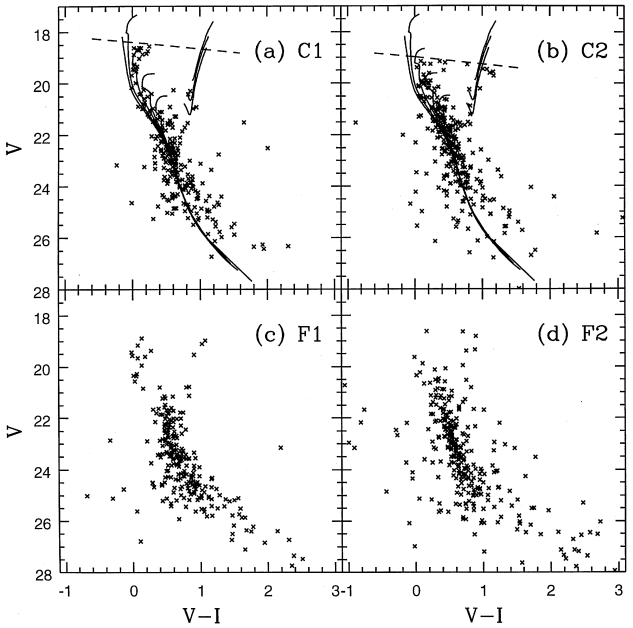


**Figure 8.** (a) The colour–magnitude diagram of stars within C1 region. Yale isochrones of 0, 200, 500, 1000 and 2000 Myr have been superposed to the data. The dashed line indicates the saturation level. (b) The same as in panel (a), but now for C2. (c) CMD for field comparison region close to C1. (d) CMD for field comparison region close to C2.

Assigning an age to C2 is harder, given the larger photometric errors and stronger saturation effects. Another problem is that the observed main sequence is a bit redder than the isochrones, suggesting a larger reddening within C2's region than elsewhere in field 2. Adjusting the reddening values in order to match the theoretical and observational main sequences and taking into account the presence of several saturated stars within C2, we can set only an *upper limit of* $\tau \lesssim 500$ Myr to the age of C2.

The derived ages for C1 and C2 are also quoted in Table 1. In the next two sections we determine the LFs and MFs for both clusters and evaluate their slopes.

## 4 LUMINOSITY AND MASS FUNCTIONS

### 4.1 Cluster luminosity functions

In Fig. 9 we show completeness-corrected LFs for C1 and C2. Field contamination was eliminated by subtracting the field LF from that within the cluster region. The field LF was taken to be the average over several control regions equidistant from the cluster. The cluster regions used for determining their LFs were circles of 8 arcsec radius centred on each cluster.

C1 seems to have a slightly steeper LF than C2. LF slopes were obtained from linear fits to the points. We obtained $\gamma = \Delta \log \Phi(M_V)/\Delta M_V = 0.19 \pm 0.03$ for C1 in the range $M_V < 6$, and $\gamma = 0.12 \pm 0.05$ for C2 in the range $M_V < 4$. The best-fitting lines are shown in the figure. Upper limits were not included in the fits. Given the small number of LF bins and the low contrast of the clusters, the differences in slope are not significant. In fact, the two LF slopes are similar in the common range used for the fits ($M_V \leq 3$). The C2 LF

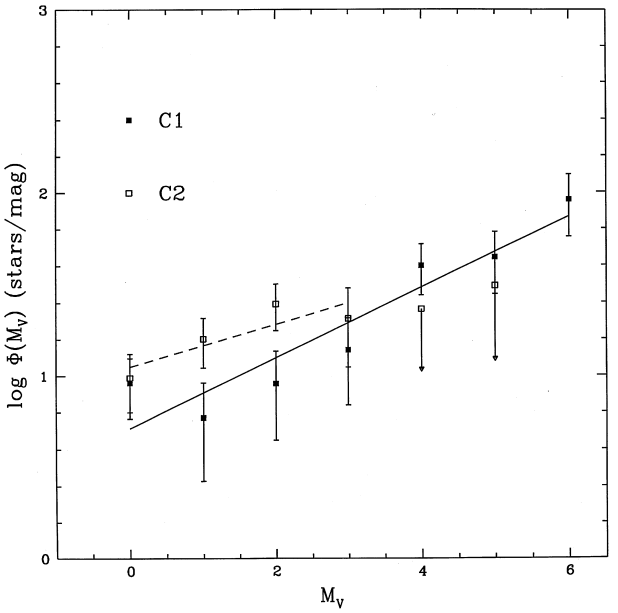


**Figure 9.** The luminosity functions of C1 and C2 are shown as solid and open squares, respectively. The error bars incorporate Poisson fluctuations as well as uncertainties in the completeness corrections and in the background subtraction. Upper limits are shown with arrows. The lines show power-law fits to the data.

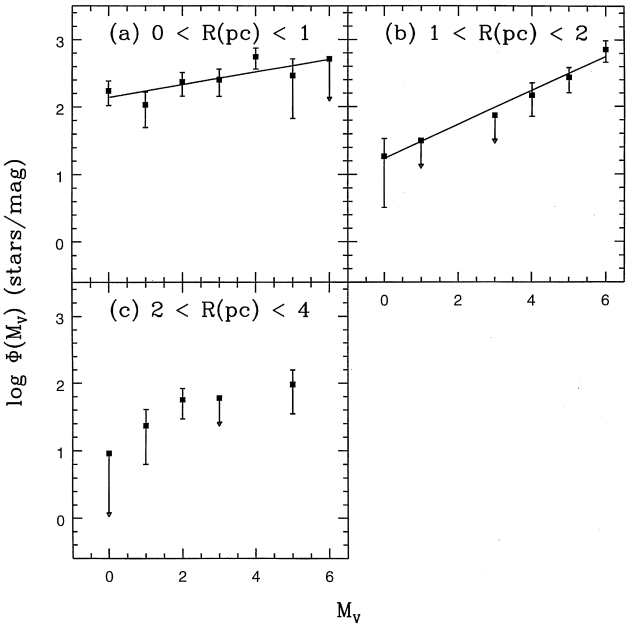


**Figure 10.** The luminosity function for C1 in different radial annuli, as indicated. The numbers in all panels are scaled to the total cluster area. Error bars again incorporate statistical uncertainties as well as completeness and background errors. Arrows correspond to upper limits. The solid line shown in the two upper panels is the best fit to a power law.

basically ends beyond that, while the C1 LF steepens. The $\gamma$ values are in agreement with that inferred from the work of Flower et al. (1980) for NGC 1868, a rich LMC cluster with an age similar to that of C1 and C2 but a larger mass. On the other hand, the inferred values for $\gamma$ are smaller than those typically fitted to younger globular clusters and to stellar associations in the LMC (Vallenari, Bomans & de Boer 1993; Will et al. 1995a; Will, Bomans & de Boer 1995b).

In Fig. 10 we show C1 LFs for three radial bins; the two first are 1-pc wide, and the last is 2-pc wide. All three LFs shown are field-subtracted and were scaled to the entire cluster area. The number of stars per unit area decreases with radius, as expected. The outermost ring contains only three bins in $M_V$ with numbers significantly above the background. This ring includes the stars that make up the excess surface brightness seen beyond $R=2$ pc in panel (b) of Fig. 6. Despite the uncertainties, the LF looks shallower in Fig. 10(c) than in Fig. 10(b), consistent with Fig. 6, where only an excess of light, not stars, is seen. In the inner rings, on the other hand, the LF becomes steeper with radius, providing evidence for mass segregation within C1. Thus the bright stars beyond $R\sim2$ pc are likely to be background stars, belonging either to the general LMC field or to some stellar association superposed to C1. In fact, C1 is situated in a rather messy border region between different clusters and associations, among them NGC 2050, LH 96, DEM 261 and NGC 157 (see catalogues by Lucke & Hodge 1970 and Davies, Elliot & Maeburn 1976). The best-fitting slopes for the LFs in the two inner rings are $\gamma=0.09\pm0.04$ and $0.25\pm0.02$. The outer ring lacks enough points for reliable fits to be made.

It was not possible to split C2's LF into radial sectors, given its smaller contrast with the background.

### 4.2 Cluster mass functions

Comparing the MFs of clusters with different masses, ages, metallicities or environments can contribute to the debate about the universality of the initial mass function (IMF) and its evolution.

The MF can be derived from the LF with the aid of a mass–luminosity ($M$–$L$) relation, which usually depends on metallicity and is often uncertain. However, the $M$–$L$ relation is reasonably well known for the typical metallicity of the LMC, $Z\sim0.008$ ([Fe/H]$\sim-0.3$), in the range of luminosities covered in this work. The mass functions for C1 and C2 are shown in Fig. 11. The $M$–$L$ conversion was based on the Yale isochrone that best fits the CMDs of the clusters. Field subtraction proceeded in the same way as with the LFs. For field stars we used the same $M$–$L$ relation as for the clusters. The derived mass of the evolved stars will obviously be in error, but these are subtracted off with the field, having little or no effect on the cluster MFs shown.

Linear fits were made to the data points leading to $\Gamma=\Delta\log\phi(M)/\Delta\log M=-1.8\pm0.7$ and $-1.2\pm0.4$ for C1 and C2, respectively. For C2, however, a single power-law fit to the MF is inappropriate, since its MF seems to be steeper for $M\gtrsim2$ M$_\odot$.

The derived slopes are subject to several sources of error. Isochrones with different metallicities or based on stellar models which incorporate convective core overshooting would change the $M$–$L$ relation and therefore the MF slopes. The effect, however, is known to be small: $\sim0.1$ in $\Gamma$ (Elson, Fall & Freeman 1989; Sagar & Richtler 1991). Unresolved binaries lead to an observed MF which is flatter than that for single stars. Sagar & Richtler (1991) investigated this issue and concluded that the amplitude of the

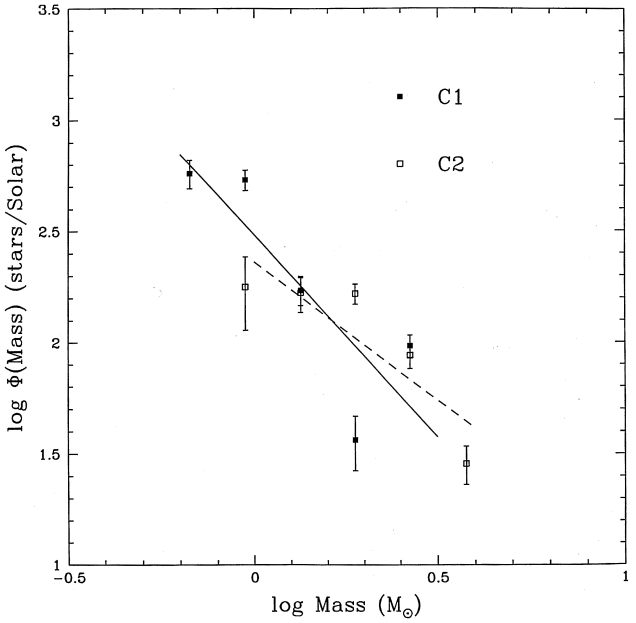


**Figure 11.** Mass functions of C1 (solid symbols) and C2 (open symbols). The error bars incorporate Poisson fluctuations as well as uncertainties in the completeness corrections and in the background subtraction. The lines show the best-fitting power laws in each case (C1: solid line; C2: dashed line).

effect is a function of the binary fraction and the MF slope itself. The observed slopes derived in this paper may be consistent with a true $\Gamma \sim -2$ and $-1.5$ for C1 and C2, respectively, if the fraction of binaries is as large as 0.5. Finally, completeness errors may distort the actual shapes of LFs and MFs, especially if mass segregation is present, as seems to be the case in C1. Given the small size of the clusters, it was impossible to split them into many annuli for which completeness and mass functions could be measured independently. Given all these uncertainties we cannot rule out a single MF shape accounting for both of them.

The LF and MF slopes are listed in Table 2, along with estimates of total luminosities ($M_V$), masses ($M$) and mass-to-light ratios ($M/L$). These latter were obtained by adding up the contributions of all non-saturated stars with $M_V \lesssim 6.5$ ($M \gtrsim 0.9$ M$_\odot$). Thus the absolute magnitude and mass estimates listed should be considered as lower limits.

The resulting MF slopes are bracketed by most of those found in the literature. These were all derived for clusters much larger than the ones studied here. Elson et al. (1989), for instance, obtained $-1.8 \lesssim \Gamma \lesssim -0.8$ for six rich young ($\tau \sim 30$–$50$ Myr) LMC clusters in the mass range $1.5 \lesssim M/\mathrm{M}_\odot \lesssim 6$. Such flat IMFs were in large contrast with the results of Mateo (1988), who found slopes ($-2.5 \lesssim \Gamma \lesssim -4.6$) for six LMC clusters spanning a wider range of ages and metallicities. Sagar & Richtler (1991) derived intermediary slopes, $\Gamma \sim -2.1$, for five LMC clusters within the mass range $2 < M/\mathrm{M}_\odot < 14$ and spanning an age range of 10–100 Myr.

More recently, and using *HST* data, Hunter et al. (1995) obtained $\Gamma = -1.22$ for R136, a $\sim 2 \times 10^4$ M$_\odot$, very young and compact system in the centre of 30 Doradus, in the range $2.8 < M/\mathrm{M}_\odot < 15$. Our results suggest flat MF slopes for low-mass LMC clusters as well.

**Table 2.** LF and MF slopes.

| Parameter | C1 | C2 |
|---|---|---|
| $\gamma = \Delta log\Phi(M_V)/\Delta log M_V$ | $0.19 \pm 0.03$ | $0.12 \pm 0.05$ |
| $\Gamma = \Delta log\phi(M)/\Delta log M$ | $-1.8 \pm 0.7$ | $-1.2 \pm 0.4$ |
| $M_V^1$ | $\sim -3.5$ | $\sim -3.5$ |
| $Mass^1$ ($M_\odot$) | $\sim 1500$ | $\sim 400$ |
| $M/L$ ($M_\odot/L_\odot$) | $\sim 0.7$ | $\sim 0.2$ |

[1]Due to stars in the range $-0.5 \lesssim M_V \lesssim 6.5$ ($0.9 \lesssim M/\mathrm{M}_\odot \lesssim 4.5$) only.

A more meaningful comparison would be with open clusters in the Galaxy. Ground-based studies include that of Sagar et al. (1986), who derived MF slopes for 11 open clusters. One of them (NGC 1778C) has an age comparable to those of C1 and C2 given in Section 3.2. Its slope is $\Gamma = -2.04 \pm 0.44$ in a mass range comparable to ours. This is consistent with C1, and marginally consistent with C2. Other more recent ground-based works have led to shallower slopes, $\Gamma \gtrsim -1$, but usually in the mass range $M \lesssim 0.5$ M$_\odot$ (Hambly et al. 1995, and references therein; Comerón, Rieke & Rieke 1996).

### 4.3 Internal dynamics

We now use the integrated properties and structural parameters listed in Tables 1 and 2 to assess the importance of dynamical effects such as two-body relaxation and tidal forces. Knowledge of the internal dynamical state of C1 and C2 may help in determining the extent to which such low-mass clusters could contribute to the field population.

Using the LMC tidal field derived by Elson, Fall & Freeman (1987), we estimate C1 and C2 to have similar tidal radii, in the range $6 \lesssim r_t \lesssim 15$ pc, implying $r_t > r_{vis}$ (see Table 1). Therefore the clusters are so far not tidally truncated. Both, however, may have experienced stronger tidal fields or had close encounters with other more massive clusters or associations during their $\gtrsim 10^8$ yr of existence.

Is two-body relaxation relevant to the internal dynamics of C1 and C2? The relaxation time-scale for stars with a mass $M$ at a distance $r$ from the centre is given by

$$t_{\mathrm{rel}} = \frac{2 \times 10^8}{\ln \Lambda} \left( \frac{r}{2 \text{ pc}} \right)^2 \left( \frac{v}{0.2 \text{ km s}^{-1}} \right) \left( \frac{\mathrm{M}_\odot}{M} \right), \quad (1)$$

where $v$ is the typical velocity of such a star within the cluster. Assuming hydrostatic equilibrium in the central regions, the central dispersion velocity in the cluster is given by

$$\sigma^2(0) \sim G \rho_0 r_c^2, \quad (2)$$

where $r_c$ is the core radius, and $\rho_0$ is the central mass density. Using the relation between projected and spatial densities given by Djorgovski (1993), we estimate $\rho_0 \sim 16$ M$_\odot$ pc$^{-3}$ for C1 and $\rho_0 \sim 6$ M$_\odot$ pc$^{-3}$ for C2. These values for the central densities imply $\sigma(0) \sim 0.4$ km s$^{-1}$ for C1 and $\sigma(0) \sim 0.2$ km s$^{-1}$ for C2. Inserting these velocities into equation (1), we infer that $t_{\mathrm{rel}} \lesssim 100$ Myr for a 1-M$_\odot$ star in the central regions of both clusters. Both C1 and C2 should therefore be relaxed in their central parts. The evidence for mass segre-

gation in C1 is consistent with that. Dispersion velocities just about twice the values inferred would disrupt the clusters in $\lesssim 50$ Myr. Given their estimated ages, C1 and C2 are probably bound.

## 5 DISCUSSION AND CONCLUSIONS

We presented $V$ and $I$ photometry of two WFPC2 fields located near the eastern end of the LMC bar. Stars as faint as $M_V \sim 7$ ($M \sim 0.8$ M$_\odot$) were detected in each of them. Each field contained one small open cluster, implying a large number density of such systems in the LMC.

C1 is roughly symmetrical in shape, and has a steep density profile and a mass function slope of $\Gamma = -1.8 \pm 0.7$. From isochrone fits, we infer an age of $\tau \sim 200$–$500$ Myr for it. Its estimated mass is $\sim 1500$ M$_\odot$, and its absolute magnitude $M_V \sim -3.5$. The derived values for the luminosity, mass, MF slope and age are mutually consistent in light of the recent stellar population synthesis models of Girardi et al. (1995). These authors use the photometric models of single stellar populations calculated by Bertelli et al. (1994) in order to revise the relation between integrated photometric properties, age and metallicity of LMC clusters. From their fig. 13, we infer that a $M \sim 2 \times 10^3$ M$_\odot$ cluster with a MF slope a bit shallower than a Salpeter one ($\Gamma = -2.35$; Salpeter 1955) would have $M_V \sim -3.5$ at an age $\tau \sim 10^8$ yr.

Marginal evidence of mass segregation within $r \lesssim 2$ pc of the centre of C1 was found. This is consistent with the short relaxation time scale expected for $M \gtrsim 1$ M$_\odot$ stars in its central regions. Tidal effects from the LMC should not be relevant; we derive $r_{\rm hl} \lesssim 1$ pc from C1's surface brightness profile, which places its member stars well inside the estimated tidal radius ($8 \lesssim r_{\rm t} \lesssim 15$ pc). Given the central density and size estimates for C1, its stars should have a maximum central velocity dispersion of $\sim 0.4$ km s$^{-1}$. It would be interesting to confirm that with observations.

C2 seems less massive but just as luminous as C1 ($M \sim 400$ M$_\odot$, $M_V \sim -3.5$). This implies flatter luminosity and mass functions. We obtain $\Gamma = -1.2 \pm 0.4$ for C2. For $M_V \lesssim 3.5$, C2's LF is similar to C1's, but it drops off for fainter magnitudes. C2 is more irregular than C1 and has shallower density and surface brightness profiles. We could derive only an upper limit of $\tau \lesssim 500$ Myr to the age of C2 based on its CMD due to saturation and reddening uncertainties. Based on the results of Girardi et al. (1995) and our mass, $M_V$ and $\Gamma$ estimates we would obtain more stringent limits: $\tau \lesssim 100$ Myr. The size of C2 was harder to quantify, given its flat profile. However, just as C1, it is also likely to be contained within its tidal radius and to have undergone significant core relaxation: $t_{\rm rel} \sim 100$ Myr for $M \gtrsim 1$ M$_\odot$ stars within the central 2 pc.

The chance discovery of two small clusters in two MDS fields within the LMC suggests that these could be more common in the LMC bar or 30 Doradus region than previously anticipated. Such systems may have significantly contributed to the field star population if they were even more common in the past and were disrupted by larger clusters or by the LMC tidal field. Even though that does not seem to be the case for C1 and C2, other similar systems may have been subjected to stronger tidal fields from both the LMC or its bar or from more massive clusters or associations. Alternatively, many such clusters might have been unbound since their birth, their member stars streaming away after a few hundred Myr. It would be interesting to confirm or not the existence of a large population of low-mass and low-luminosity clusters in the LMC with other observations using the high resolution of *HST*.

## ACKNOWLEDGMENTS

We thank Sally Oey and Eduardo Bica for their help and useful discussions. BXS is grateful to the hospitality of the Institute of Astronomy, where part of this work was carried out.

## REFERENCES

Bertelli G., Bressan A., Chiosi C., Fagotto F., 1994, A&AS, 106, 275
Comerón F., Rieke G. H., Rieke M. J., 1996, ApJ, 473, 294
Davies R. D., Elliot K. H., Meaburn J., 1976, Mem. RAS, 81, 89
de Marchi G., Paresce F., 1995a, A&A, 304, 202
de Marchi G., Paresce F., 1995b, A&A, 304, 211
Djorgovski S., 1993, in ASP Conf. Ser. Vol. 50, The Structure and Dynamics of Globular Clusters. Astron. Soc. Pac., San Francisco, p. 373
Elson R. A. W., Fall S. M., 1985, PASP, 97, 594
Elson R. A. W., Fall S. M., Freeman K. C., 1987, ApJ, 323, 54
Elson R. A. W., Fall S. M., Freeman K. C., 1989, ApJ, 336, 734
Elson R. A. W., Gilmore G., Santiago B. X., Casertano S., 1995, AJ, 110, 682
Elson R. A. W., Gilmore G. F., Santiago B. X., 1997, MNRAS, 289, 157
Flower P. J., Geisler D., Hodge P., Olszewski E. W., 1980, ApJ, 235, 769
Girardi L., Chiosi C., Bertelli G., Bressan A., 1995, A&A, 298, 87
Green E. M., Demarque P., King C. R., 1987, Yale Univ. Transactions, Yale Univ. Observatory
Hambly N. C., Steele I. A., Hawkins M. R. S., Jameson R. F., 1995, MNRAS, 273, 505
Hodge P., 1988, PASP, 100, 1051
Holtzmann J. A. et al., 1995a, PASP, 107, 156
Holtzmann J. A. et al., 1995b, PASP, 107, 1065
Hunter D. A., Shaya E. J., Holtzmann J. A., Light R. M., 1995, ApJ, 448, 179
Hunter D. A., O'Neil E. J., Lynds R., Shaya E. J., Groth E. J., Holtzmann J. A., 1996, ApJ, 459, L27
Larson R. B., 1991, in Falgarone E., Boulanger F., Duvert G., eds, Proc. IAU Symp. 147, Fragmentation of Molecular Clouds and Star Formation. Kluwer, Dordrecht, p. 261
Larson R. B., 1992, MNRAS, 256, 641
Lucke P. B., Hodge P. W., 1970, AJ, 75, 171
Mateo M., 1988, apJ, 331, 261
McClure R. D. et al., 1986, ApJ, 307, L49
Olszewski E., Schommer R., Suntzeff F., Adorf H.-M., Kirshner R., 1991, ApJ, 380, L23
Sagar R., Richtler T., 1991, A&A, 250, 324
Sagar R., Piskunov A. E., Myakutin V. I., Joshi U. C., 1986, MNRAS, 220, 383
Salpeter E. E., 1955, ApJ, 121, 161
Santiago B. X., Elson R. A. W., Gilmore G. F., 1996, MNRAS, 281, 1363
Stetson P. B., 1987, PASP, 99, 191
Vallenari A., Bomans D. J., de Boer K. S., 1993, A&A, 268, 137
Will J.-M., Vázquez R. A., Feinstein A., Seggewiss W., 1995a, A&A, 301, 396
Will J.-M., Bomans D. J., de Boer K. S., 1995b, A&A, 295, 54